

Multi-photon production in e^+e^- collisions at $\sqrt{s} = 189$ GeV

The OPAL Collaboration

Abstract

The process $e^+e^- \rightarrow \gamma\gamma(\gamma)$ is studied using data recorded with the OPAL detector at LEP. The data sample taken at a centre-of-mass energy of 189 GeV corresponds to a total integrated luminosity of 178 pb^{-1} . The measured cross-section agrees well with the expectation from QED. A fit to the angular distribution is used to obtain improved limits at 95% CL on the QED cut-off parameters: $\Lambda_+ > 304 \text{ GeV}$ and $\Lambda_- > 295 \text{ GeV}$ as well as a mass limit for an excited electron, $M_{e^*} > 306 \text{ GeV}$ assuming equal $e^*e\gamma$ and $ee\gamma$ couplings. Graviton exchange in the context of theories with higher dimensions is excluded for scales $G_+ < 660 \text{ GeV}$ and $G_- < 634 \text{ GeV}$. No evidence for resonance production is found in the invariant mass spectrum of photon pairs. Limits are obtained for the cross-section times branching ratio for a resonance decaying into two photons and produced in association with another photon.

(To be submitted to Phys. Lett.)

The OPAL Collaboration

G. Abbiendi², K. Ackerstaff⁸, G. Alexander²³, J. Allison¹⁶, K.J. Anderson⁹, S. Anderson¹²,
S. Arcelli¹⁷, S. Asai²⁴, S.F. Ashby¹, D. Axen²⁹, G. Azuelos^{18,a}, A.H. Ball⁸, E. Barberio⁸,
R.J. Barlow¹⁶, J.R. Batley⁵, S. Baumann³, J. Bechtluft¹⁴, T. Behnke²⁷, K.W. Bell²⁰, G. Bella²³,
A. Bellerive⁹, S. Bentvelsen⁸, S. Bethke¹⁴, S. Betts¹⁵, O. Biebel¹⁴, A. Biguzzi⁵, I.J. Bloodworth¹,
P. Bock¹¹, J. Böhme¹⁴, O. Boeriu¹⁰, D. Bonacorsi², M. Boutemour³³, S. Braibant⁸,
P. Bright-Thomas¹, L. Brigliadori², R.M. Brown²⁰, H.J. Burckhart⁸, P. Capiluppi²,
R.K. Carnegie⁶, A.A. Carter¹³, J.R. Carter⁵, C.Y. Chang¹⁷, D.G. Charlton^{1,b}, D. Chrisman⁴,
C. Ciocca², P.E.L. Clarke¹⁵, E. Clay¹⁵, I. Cohen²³, J.E. Conboy¹⁵, O.C. Cooke⁸, J. Couchman¹⁵,
C. Couyoumtzelis¹³, R.L. Coxe⁹, M. Cuffiani², S. Dado²², G.M. Dallavalle², S. Dallison¹⁶,
R. Davis³⁰, S. De Jong¹², A. de Roeck⁸, P. Dervan¹⁵, K. Desch²⁷, B. Dienes^{32,h}, M.S. Dixit⁷,
M. Donkers⁶, J. Dubbert³³, E. Duchovni²⁶, G. Duckeck³³, I.P. Duerdoth¹⁶, P.G. Estabrooks⁶,
E. Etzion²³, F. Fabbri², A. Fanfani², M. Fanti², A.A. Faust³⁰, L. Feld¹⁰, P. Ferrari¹²,
F. Fiedler²⁷, M. Fierro², I. Fleck¹⁰, A. Frey⁸, A. Fürtjes⁸, D.I. Futyan¹⁶, P. Gagnon⁷,
J.W. Gary⁴, G. Gaycken²⁷, C. Geich-Gimbel³, G. Giacomelli², P. Giacomelli², W.R. Gibson¹³,
D.M. Gingrich^{30,a}, D. Glenzinski⁹, J. Goldberg²², W. Gorn⁴, C. Grandi², K. Graham²⁸,
E. Gross²⁶, J. Grunhaus²³, M. Gruwé²⁷, C. Hajdu³¹, G.G. Hanson¹², M. Hansroul⁸, M. Hapke¹³,
K. Harder²⁷, A. Harel²², C.K. Hargrove⁷, M. Harin-Dirac⁴, M. Hauschild⁸, C.M. Hawkes¹,
R. Hawkings²⁷, R.J. Hemingway⁶, G. Herten¹⁰, R.D. Heuer²⁷, M.D. Hildreth⁸, J.C. Hill⁵,
P.R. Hobson²⁵, A. Hocker⁹, K. Hoffman⁸, R.J. Homer¹, A.K. Honma^{28,a}, D. Horváth^{31,c},
K.R. Hossain³⁰, R. Howard²⁹, P. Hütemeyer²⁷, P. Igo-Kemenes¹¹, D.C. Imrie²⁵, K. Ishii²⁴,
F.R. Jacob²⁰, A. Jawahery¹⁷, H. Jeremie¹⁸, M. Jimack¹, C.R. Jones⁵, P. Jovanovic¹, T.R. Junk⁶,
N. Kanaya²⁴, J. Kanzaki²⁴, D. Karlen⁶, V. Kartvelishvili¹⁶, K. Kawagoe²⁴, T. Kawamoto²⁴,
P.I. Kayal³⁰, R.K. Keeler²⁸, R.G. Kellogg¹⁷, B.W. Kennedy²⁰, D.H. Kim¹⁹, A. Klier²⁶,
T. Kobayashi²⁴, M. Kobel^{3,d}, T.P. Kokott³, M. Kolrep¹⁰, S. Komamiya²⁴, R.V. Kowalewski²⁸,
T. Kress⁴, P. Krieger⁶, J. von Krogh¹¹, T. Kuhl³, P. Kyberd¹³, G.D. Lafferty¹⁶, H. Landsman²²,
D. Lanske¹⁴, J. Lauber¹⁵, I. Lawson²⁸, J.G. Layter⁴, D. Lellouch²⁶, J. Letts¹², L. Levinson²⁶,
R. Liebisch¹¹, J. Lillich¹⁰, B. List⁸, C. Littlewood⁵, A.W. Lloyd¹, S.L. Lloyd¹³, F.K. Loebinger¹⁶,
G.D. Long²⁸, M.J. Losty⁷, J. Lu²⁹, J. Ludwig¹⁰, D. Liu¹², A. Macchiolo¹⁸, A. Macpherson³⁰,
W. Mader³, M. Mannelli⁸, S. Marcellini², T.E. Marchant¹⁶, A.J. Martin¹³, J.P. Martin¹⁸,
G. Martinez¹⁷, T. Mashimo²⁴, P. Mättig²⁶, W.J. McDonald³⁰, J. McKenna²⁹, E.A. Mckigney¹⁵,
T.J. McMahon¹, R.A. McPherson²⁸, F. Meijers⁸, P. Mendez-Lorenzo³³, F.S. Merritt⁹, H. Mes⁷,
I. Meyer⁵, A. Michelini², S. Mihara²⁴, G. Mikenberg²⁶, D.J. Miller¹⁵, W. Mohr¹⁰, A. Montanari²,
T. Mori²⁴, K. Nagai⁸, I. Nakamura²⁴, H.A. Neal^{12,g}, R. Nisius⁸, S.W. O’Neale¹, F.G. Oakham⁷,
F. Odorici², H.O. Ogren¹², A. Okpara¹¹, M.J. Oreglia⁹, S. Orito²⁴, G. Pásztor³¹, J.R. Pater¹⁶,
G.N. Patrick²⁰, J. Patt¹⁰, R. Perez-Ochoa⁸, S. Petzold²⁷, P. Pfeifenschneider¹⁴, J.E. Pilcher⁹,
J. Pinfold³⁰, D.E. Plane⁸, P. Poffenberger²⁸, B. Poli², J. Polok⁸, M. Przybycień^{8,e}, A. Quadt⁸,
C. Rembser⁸, H. Rick⁸, S. Robertson²⁸, S.A. Robins²², N. Rodning³⁰, J.M. Roney²⁸, S. Rosati³,
K. Roscoe¹⁶, A.M. Rossi², Y. Rozen²², K. Runge¹⁰, O. Runolfsson⁸, D.R. Rust¹², K. Sachs¹⁰,
T. Saeki²⁴, O. Sahr³³, W.M. Sang²⁵, E.K.G. Sarkisyan²³, C. Sbarra²⁹, A.D. Schaile³³,
O. Schaile³³, P. Scharff-Hansen⁸, J. Schieck¹¹, S. Schmitt¹¹, A. Schöning⁸, M. Schröder⁸,
M. Schumacher³, C. Schwick⁸, W.G. Scott²⁰, R. Seuster¹⁴, T.G. Shears⁸, B.C. Shen⁴,
C.H. Shepherd-Themistocleous⁵, P. Sherwood¹⁵, G.P. Siroli², A. Skuja¹⁷, A.M. Smith⁸,
G.A. Snow¹⁷, R. Sobie²⁸, S. Söldner-Rembold^{10,f}, S. Spagnolo²⁰, M. Sproston²⁰, A. Stahl³,

K. Stephens¹⁶, K. Stoll¹⁰, D. Strom¹⁹, R. Ströhmer³³, B. Surrow⁸, S.D. Talbot¹, P. Taras¹⁸,
S. Tarem²², R. Teuscher⁹, M. Thiergen¹⁰, J. Thomas¹⁵, M.A. Thomson⁸, E. Torrence⁸,
S. Towers⁶, T. Trefzger³³, I. Trigger¹⁸, Z. Trócsányi^{32,h}, E. Tsur²³, M.F. Turner-Watson¹,
I. Ueda²⁴, R. Van Kooten¹², P. Vannerem¹⁰, M. Verzocchi⁸, H. Voss³, F. Wäckerle¹⁰,
A. Wagner²⁷, D. Waller⁶, C.P. Ward⁵, D.R. Ward⁵, P.M. Watkins¹, A.T. Watson¹,
N.K. Watson¹, P.S. Wells⁸, N. Wermes³, D. Wetterling¹¹, J.S. White⁶, G.W. Wilson¹⁶,
J.A. Wilson¹, T.R. Wyatt¹⁶, S. Yamashita²⁴, V. Zacek¹⁸, D. Zer-Zion⁸

¹School of Physics and Astronomy, University of Birmingham, Birmingham B15 2TT, UK

²Dipartimento di Fisica dell' Università di Bologna and INFN, I-40126 Bologna, Italy

³Physikalisches Institut, Universität Bonn, D-53115 Bonn, Germany

⁴Department of Physics, University of California, Riverside CA 92521, USA

⁵Cavendish Laboratory, Cambridge CB3 0HE, UK

⁶Ottawa-Carleton Institute for Physics, Department of Physics, Carleton University, Ottawa, Ontario K1S 5B6, Canada

⁷Centre for Research in Particle Physics, Carleton University, Ottawa, Ontario K1S 5B6, Canada

⁸CERN, European Organisation for Particle Physics, CH-1211 Geneva 23, Switzerland

⁹Enrico Fermi Institute and Department of Physics, University of Chicago, Chicago IL 60637, USA

¹⁰Fakultät für Physik, Albert Ludwigs Universität, D-79104 Freiburg, Germany

¹¹Physikalisches Institut, Universität Heidelberg, D-69120 Heidelberg, Germany

¹²Indiana University, Department of Physics, Swain Hall West 117, Bloomington IN 47405, USA

¹³Queen Mary and Westfield College, University of London, London E1 4NS, UK

¹⁴Technische Hochschule Aachen, III Physikalisches Institut, Sommerfeldstrasse 26-28, D-52056 Aachen, Germany

¹⁵University College London, London WC1E 6BT, UK

¹⁶Department of Physics, Schuster Laboratory, The University, Manchester M13 9PL, UK

¹⁷Department of Physics, University of Maryland, College Park, MD 20742, USA

¹⁸Laboratoire de Physique Nucléaire, Université de Montréal, Montréal, Quebec H3C 3J7, Canada

¹⁹University of Oregon, Department of Physics, Eugene OR 97403, USA

²⁰CLRC Rutherford Appleton Laboratory, Chilton, Didcot, Oxfordshire OX11 0QX, UK

²²Department of Physics, Technion-Israel Institute of Technology, Haifa 32000, Israel

²³Department of Physics and Astronomy, Tel Aviv University, Tel Aviv 69978, Israel

²⁴International Centre for Elementary Particle Physics and Department of Physics, University of Tokyo, Tokyo 113-0033, and Kobe University, Kobe 657-8501, Japan

²⁵Institute of Physical and Environmental Sciences, Brunel University, Uxbridge, Middlesex UB8 3PH, UK

²⁶Particle Physics Department, Weizmann Institute of Science, Rehovot 76100, Israel

²⁷Universität Hamburg/DESY, II Institut für Experimental Physik, Notkestrasse 85, D-22607 Hamburg, Germany

²⁸University of Victoria, Department of Physics, P O Box 3055, Victoria BC V8W 3P6, Canada

²⁹University of British Columbia, Department of Physics, Vancouver BC V6T 1Z1, Canada

³⁰University of Alberta, Department of Physics, Edmonton AB T6G 2J1, Canada

³¹Research Institute for Particle and Nuclear Physics, H-1525 Budapest, P O Box 49, Hungary

³²Institute of Nuclear Research, H-4001 Debrecen, P O Box 51, Hungary

³³Ludwigs-Maximilians-Universität München, Sektion Physik, Am Coulombwall 1, D-85748 Garching, Germany

^a and at TRIUMF, Vancouver, Canada V6T 2A3

^b and Royal Society University Research Fellow

^c and Institute of Nuclear Research, Debrecen, Hungary

^d on leave of absence from the University of Freiburg

^e and University of Mining and Metallurgy, Cracow

^f and Heisenberg Fellow

^g now at Yale University, Dept of Physics, New Haven, USA

^h and Department of Experimental Physics, Lajos Kossuth University, Debrecen, Hungary.

1 Introduction

This paper reports a study of the process $e^+e^- \rightarrow \gamma\gamma(\gamma)$ using data recorded with the OPAL detector at LEP at an average centre-of-mass energy of 188.63 ± 0.04 GeV with an integrated luminosity of 178.3 ± 0.4 pb $^{-1}$. This is one of the few processes dominated by QED even at high LEP energies. Since the differential cross-section is well known from QED [1, 2], any deviation from this expectation hints at non-standard physics processes contributing to these photonic final states. Any non-QED effects within the general framework of effective Lagrangian theory are expected to increase with centre-of-mass energy [3]. A comparison of the measured photon angular distribution with the QED expectation can be used to place limits on the QED cut-off parameters Λ_{\pm} , contact interactions ($e^+e^-\gamma\gamma$) and non-standard $e^+e^-\gamma$ -couplings as described in Section 3. The possible existence of an excited electron e^* which would change the angular distribution [4], is investigated as well as the possibility of graviton exchange in the context of theories with higher dimensions [5]. In addition, a search is made for the production of a resonance X via $e^+e^- \rightarrow X\gamma$ followed by the decay $X \rightarrow \gamma\gamma$, using the invariant mass spectrum of photon pairs in three-photon final states. The process $e^+e^- \rightarrow \gamma\gamma(\gamma)$ has been analysed previously at lower energies [6, 7, 8, 9, 10]. The selection presented in this paper is almost unchanged with respect to the previous OPAL analysis at $\sqrt{s} = 183$ GeV [7].

2 The OPAL detector and Monte Carlo samples

A detailed description of the OPAL detector can be found in Ref. [11]. The polar angle θ is measured with respect to the electron beam direction and ϕ is the azimuthal angle. For this analysis the most important detector component is the electromagnetic calorimeter (ECAL) which is divided into two parts, the barrel and the endcaps. The barrel covers polar angles with $|\cos\theta| < 0.82$ and consists of 9440 lead-glass blocks in a quasi-pointing geometry. The two endcaps cover the polar angle range $0.81 < |\cos\theta| < 0.98$ and each consists of 1132 blocks. For beam-energy photons, the spatial resolution is about 11 mm, corresponding to 0.2° in θ , and the energy resolution is about 2% in the barrel and 3 – 5% in the endcaps, depending on the polar angle. The ECAL surrounds the tracking chambers. Hit information from the central jet chamber CJ and the central vertex drift chamber CV is used to reject events which are consistent with having charged particles coming from the interaction point. Outside the ECAL is the hadronic calorimeter HCAL which is incorporated into the magnet yoke, and beyond that are the muon chambers. Both the HCAL and the muon chambers are used to reject cosmic ray events.

Various Monte Carlo samples are used to study the selection efficiency and expected background contributions. For the signal process $e^+e^- \rightarrow \gamma\gamma(\gamma)$ the RADCOR [2] generator is used while FGAM [12] is used for $e^+e^- \rightarrow \gamma\gamma\gamma\gamma$. FGAM does not take into account the electron mass leading to a divergent cross-section at small angles and hence can not be used if at least one photon is along the beam axis. The Bhabha process is simulated using BHWIDE [13] and TEEGG [14]. The process $e^+e^- \rightarrow \bar{\nu}\nu\gamma(\gamma)$ is simulated using KORALZ [15]. All samples were processed through the OPAL detector simulation program [16] and reconstructed in the same way as the data.

3 Cross-section for the process $e^+e^- \rightarrow \gamma\gamma$

The Born-level differential cross-section for the process $e^+e^- \rightarrow \gamma\gamma$ in the relativistic limit of lowest order QED is given by [17]

$$\left(\frac{d\sigma}{d\Omega}\right)_{\text{Born}} = \frac{\alpha^2}{s} \frac{1 + \cos^2 \theta}{1 - \cos^2 \theta}, \quad (1)$$

where s denotes the square of the centre-of-mass energy, α is the fine-structure constant and θ is the polar angle of one photon. Since the two photons are identical particles, the event angle is defined by convention such that $\cos \theta$ is positive.

In a multi-photon event, it is important to choose an appropriate definition of the event angle. The event angle is not uniquely defined since the two highest-energy photons in general are not exactly back-to-back. The event angle $\cos \theta^*$ used in this paper is defined as

$$\cos \theta^* = \left| \sin \frac{\theta_1 - \theta_2}{2} \right| \bigg/ \left(\sin \frac{\theta_1 + \theta_2}{2} \right), \quad (2)$$

where θ_1 and θ_2 are the polar angles of the two highest-energy photons. This definition was chosen such that the deviations in the angular distribution with respect to the Born level are small, in this case between 3 and 6% for $\cos \theta^* < 0.99$, as was shown in Ref. [6]. For two-photon final states, $\cos \theta^*$ is identical to $|\cos \theta|$ and for three-photon events in which the third photon is along the beam direction, θ^* is equivalent to the scattering angle in the centre-of-mass system of the two observed photons. Since the angular definition is based on the two highest-energy photons, events with one of these escaping detection along the beam axis are rejected from the analysis. The observed angular distribution is corrected for these higher-order effects using $\mathcal{O}(\alpha^3)$ Monte Carlo studies in order that it can be directly compared to the following model expectations given in lowest order.

In Ref. [1], possible deviations from the QED cross-section for Bhabha and Møller scattering are parametrised in terms of cut-off parameters Λ_{\pm} . These parameters correspond to a short-range exponential term added to the Coulomb potential. This ansatz leads to modifications of the photon angular distribution of the form

$$\left(\frac{d\sigma}{d\Omega}\right)_{\Lambda_{\pm}} = \left(\frac{d\sigma}{d\Omega}\right)_{\text{Born}} \pm \frac{\alpha^2 s}{2\Lambda_{\pm}^4} (1 + \cos^2 \theta). \quad (3)$$

Alternatively, in terms of effective Lagrangian theory, a gauge-invariant operator may be added to QED. Depending on the dimension of the operator, different deviations from QED can be formulated [3]. Contact interactions ($\gamma\gamma e^+e^-$) or non-standard γe^+e^- couplings described by operators of dimension 6, 7 or 8 lead to angular distributions with different mass scales Λ . In most cases these deviations are functionally similar [6]. Therefore, only the cross-section predicted by a dimension-7 Lagrangian, given by

$$\left(\frac{d\sigma}{d\Omega}\right)_{\Lambda'} = \left(\frac{d\sigma}{d\Omega}\right)_{\text{Born}} + \frac{s^2}{32\pi} \frac{1}{\Lambda'^6}, \quad (4)$$

is studied here. Limits on mass scales for Lagrangians of dimension 6 and 8 can easily be derived from limits on Λ_{\pm} and Λ' [6].

The existence of an excited electron e^* with an $e^*e\gamma$ coupling would contribute to the photon production process via t -channel exchange. The resulting deviation from $\left(\frac{d\sigma}{d\Omega}\right)_{\text{Born}}$ depends on the e^* mass M_{e^*} and the coupling constant κ of the $e^*e\gamma$ vertex relative to the $ee\gamma$ vertex [4]:

$$\left(\frac{d\sigma}{d\Omega}\right)_{e^*} = \left(\frac{d\sigma}{d\Omega}\right)_{\text{Born}} + f(M_{e^*}, \kappa, s, \cos\theta). \quad (5)$$

The function f is explicitly given in Ref. [6]. In the limit $M_{e^*} \gg \sqrt{s}$, $\left(\frac{d\sigma}{d\Omega}\right)_{e^*}$ approaches $\left(\frac{d\sigma}{d\Omega}\right)_{\Lambda_{\pm}}$ with the mass related to the cut-off parameter by $M_{e^*} = \sqrt{\kappa} \Lambda_+$.

Recent theories [5] have pointed out that the graviton G might propagate in a higher-dimensional space where additional dimensions are compactified while other Standard Model particles are confined to the usual 3+1 space-time dimensions. This would allow the large Planck scale M_{Pl} with an effective scale M_{D} of order of the electroweak scale ($\mathcal{O}(10^{2-3}\text{GeV})$) via $M_{\text{Pl}}^2 = R^n M_{\text{D}}^{n+2}$, where R is the compactification radius for n higher dimensions. Although the contribution from $e^+e^- \rightarrow G^* \rightarrow \gamma\gamma$ for a single mode is small compared to the Standard Model contribution, the very large number of possible excitation modes in the extra dimensions might lead to a measurable effect on the resulting differential cross-section, given by [18]

$$\left(\frac{d\sigma}{d\Omega}\right)_{G_{\pm}} = \left(\frac{d\sigma}{d\Omega}\right)_{\text{Born}} \pm \frac{\alpha s}{\pi^2} G_{\pm}^{-4} (1 + \cos^2\theta) + \frac{s^3}{64\pi^2} G_{\pm}^{-8} (1 - \cos^4\theta), \quad (6)$$

where G_{\pm} are scale parameters of order of the effective scale M_{D} .

4 Event selection

A) Preselection

The preselection has only small changes compared to our previous analysis [7]. Events are selected if they have two or more ECAL clusters within the polar-angle range $|\cos\theta| < 0.97$ each with more than 1 GeV of deposited energy uncorrected for possible energy loss in the material before the ECAL. Other energies used in the analysis are corrected for these losses. A cluster must consist of at least two lead-glass blocks. This preselection is tightened by requiring a total energy in the ECAL of at least 10% of the centre-of-mass energy.

B) Rejection of non-physics backgrounds

A cosmic-ray particle can pass through the hadronic and electromagnetic calorimeters without producing a reconstructed track in the central tracking chambers. The requirements to reject these events are the same as in our previous analysis. We reject events with 3 or more track segments found in the muon chambers. In the case of fewer than three such track segments, the event rejection depends on the highest-energy HCAL cluster of the event. Events are rejected if this HCAL cluster is separated from each of the photon candidates by more than 10° in azimuth

and has at least 1 GeV of deposited energy in the case of one or two muon-track segments, or at least 15% of the observed ECAL energy if no muon-track segments are found.

Another type of background is consistent with well localised electronic noise in the ECAL. The cuts used to reject these events are slightly relaxed compared to our previous analysis to account for the larger cluster size due to the higher centre-of-mass energy. An event is rejected if one of these accumulations consists of more than 14 ECAL clusters or has an extent of more than 0.5 rad in θ or 0.5 rad/sin θ in ϕ .

C) Kinematic requirements

The selection is based primarily on the requirement of small missing energy and small missing transverse momentum and is unchanged with respect to our previous analysis. Non-physics background and events containing invisible particles or having only a small energy deposit in the ECAL are rejected by this selection. In particular, events from the Standard Model process $e^+e^- \rightarrow \bar{\nu}\nu\gamma\gamma$ fail this selection. Better resolution on quantities such as the total longitudinal or transverse momentum of an event is obtained by using cluster angles and three-body kinematics where possible, rather than using measured energies. Therefore the event sample is divided into four classes, *I*–*IV*. The classes are distinguished by the number of photon candidates N_γ , the acollinearity angle ξ_{acol} , and the aplanarity angle ξ_{aplan} :

$$\xi_{\text{acol}} = 180^\circ - \alpha_{12} \quad (7)$$

$$\xi_{\text{aplan}} = 360^\circ - (\alpha_{12} + \alpha_{13} + \alpha_{23}), \quad (8)$$

where α_{ij} is the angle between clusters i and j and the indices are ordered by decreasing cluster energy.

All events having $\xi_{\text{acol}} < 10^\circ$ (i.e. with the two highest-energy clusters almost collinear) are assigned to class *I*, independent of the number of photon candidates. More than 90% of the events fall in this class. Acollinear events ($\xi_{\text{acol}} > 10^\circ$) are separated into three classes. Events with $N_\gamma = 2$ are assigned to class *II*, typically containing an energetic photon that escapes

Event class	<i>I</i>	<i>II</i>	<i>III</i>	<i>IV</i>
Number of photon candidates	$N_\gamma \geq 2$	$N_\gamma = 2$	$N_\gamma = 3$	$N_\gamma \geq 3$
Acollinearity	$\xi_{\text{acol}} < 10^\circ$	$\xi_{\text{acol}} > 10^\circ$	$\xi_{\text{acol}} > 10^\circ$	$\xi_{\text{acol}} > 10^\circ$
Aplanarity			$\xi_{\text{aplan}} < 0.1^\circ$	$\xi_{\text{aplan}} > 0.1^\circ$
Energy sum	$E_S^I > 0.6\sqrt{s}$	$E_S^{II} > 0.6\sqrt{s}$	$E_S^{III} > 0.6\sqrt{s}$	$E_S^{IV} > 0.6\sqrt{s}$
Transverse momentum		$\mathcal{B} < 0.2$	$p_t < 0.1\sqrt{s}$	$p_t < 0.1\sqrt{s}$
Longitudinal momentum		$E_{\text{lost}} < E_1, E_2$	$p_l < E_1, E_2$	$p_l < E_1, E_2$

Table 1: Summary of the kinematic cuts. The upper part of the table describes the definition of the four event classes, the lower part describes the applied cuts. For definition of the variables see the text. In the case of more than three observed photons in class *IV* there is no requirement on the aplanarity.

detection near the beam axis ($|\cos\theta| > 0.97$). Planar events ($\xi_{\text{aplan}} < 0.1^\circ$) with exactly 3 observed photon candidates are assigned to class *III*. The remaining events, i.e. aplanar three-photon events ($\xi_{\text{aplan}} > 0.1^\circ$) and events with more than three observed photon candidates are assigned to class *IV*. Classes *III* and *IV* are distinguished for two reasons. Firstly, the main signal Monte Carlo generator calculates only events with up to three photons, class *IV* events are not described by this program. Secondly, for class *III* events, three-body kinematics can be used to calculate the photon energies from the angles, to determine the invariant masses of photon pairs. This is not possible for class *IV* events. The event class definitions are summarised in Table 1.

Events in all classes are required to meet the following criteria:

- C1** The energy sum of all observed ECAL clusters must be more than 60% of the centre-of-mass energy and the transverse momentum of the event must be less than 10% of the centre-of-mass energy.
- C2** The longitudinal momentum of the event must be smaller than the energy of each of the two highest-energy clusters to ensure that the two highest-energy photons in the event are observed.

For class *I* events it is assumed that missing energy is negligible due to the collinearity. There is only one cut applied to the sum of the two highest cluster energies $E_S^I = E_1 + E_2$. The distribution of E_S^I/\sqrt{s} is shown in Figure 1. Events are selected if $E_S^I > 0.6\sqrt{s}$.

For class *II* events three-body kinematics can be used to calculate missing energy assuming a third unobserved photon with $|\cos\theta| = 1$. The missing longitudinal momentum can be estimated as $E_{\text{lost}} = \sqrt{s}/[1 + (\sin\theta_1 + \sin\theta_2)/|\sin(\theta_1 + \theta_2)|]$ and the transverse momentum can be approximated by the imbalance $\mathcal{B} = (\sin\theta_1 + \sin\theta_2)|\cos[(\phi_1 - \phi_2)/2]|$, where θ_1, θ_2 and ϕ_1, ϕ_2 are the angles of the observed clusters. The energy sum $E_S^{II} = E_1 + E_2 + E_{\text{lost}}$ is calculated by summing the two observed cluster energies and the missing energy. Events are selected if $E_S^{II} > 0.6\sqrt{s}$, $\mathcal{B} < 0.2$ and E_{lost} is less than both E_1 and E_2 . This last requirement ensures that the two highest-energy photons are those observed. Figure 2a shows the distribution of E_S^{II}/\sqrt{s} for the data before and after the cut on \mathcal{B} , compared with the signal Monte Carlo.

For events in classes *III* and *IV*, the cluster energies must be used in addition to the cluster angles in calculating the transverse and longitudinal momenta (p_t, p_l) of the system. The energy sum $E_S^{III} = \sum_{i=1}^{N_\gamma} E_i + p_l$ is calculated by adding p_l to the cluster energies E_i . Events are selected if $E_S^{III} > 0.6\sqrt{s}$ and $p_t < 0.1\sqrt{s}$. Again, the missing energy along the beam axis, now determined by p_l , must be smaller than the energies of the two highest-energy clusters. Figure 2b shows the distribution of E_S^{III}/\sqrt{s} for the data before and after the cut on p_t , compared with the signal Monte Carlo.

The non-physics background is reduced to a negligible level after the above kinematic requirements which are summarised in Table 1.

D) Charged event rejection

Bhabha events, for example, have electromagnetic cluster characteristics similar to $\gamma\gamma(\gamma)$ events, but can be distinguished by the presence of tracks in the central tracking chambers. The rejection of all events having tracks in the central tracking chambers, however, would lead to an efficiency loss because of photon conversions. Nevertheless, contributions from any channel with primary charged tracks must be reduced to a negligible level for this analysis. To achieve this, for each cluster, hits in the inner part of the drift chambers CV and CJ which are associated in ϕ with the cluster are counted. If the number of such hits in CV (CJ) is above a θ -dependent threshold, as described in [6], a CV (CJ) token is assigned to the cluster. There are three ways to reject an event:

1. The single veto rejects events with both a CV and a CJ token assigned to the same cluster.
2. The double veto rejects events with either a CV or a CJ token assigned to the two highest-energy clusters.
3. Events are rejected if there is a reconstructed track separated by more than 10° in azimuth from all photon candidates.

5 Corrections and systematic errors

Table 2 shows the number of selected events from the data, the signal Monte Carlo and the major background sources after the different selection cuts. Other processes contribute only a small number of events [7]. The preselected data have some contribution from non-physics backgrounds and from the process $e^+e^- \rightarrow q\bar{q}$ until the kinematic cuts are applied. There is little efficiency loss up to this point. The restriction on the missing longitudinal momentum (E_{lost} for class II) rejects events with a high-energy photon escaping along the beam axis. About 97% of the remaining sample consists of Bhabha events and is well described by the

Cut		Data	MC	$\gamma\gamma(\gamma)$	$e^+e^-(\gamma)$	$e\gamma(e)$	$\nu\bar{\nu}\gamma\gamma$
A)	Preselection	116 129	90 576	2 297	82 157	6 078	44
B)	Non-physics bg. reject.	96 307	90 393	2 296	82 014	6 039	44
C1)	Kinematic requirements	88 715	87 429	2 273	79 848	5 305	3.2
C2)	$E_{\text{lost}}, p_l < E_1, E_2$	78 782	79 460	2 109	77 183	168	0.05
D)	Charged event rejection	1 740	1 777	1 775	0.4	0.9	0.04
Statistical errors		42	8	8	0.2	0.4	0.01

Table 2: Number of selected events after the different cuts described in the text. The numbers are given for the data and the sum of Monte Carlo samples with the breakdown by final states given in the following columns. The BHWIDE generator is labelled by $e^+e^-(\gamma)$ and TEEGG by $e\gamma(e)$. All Monte Carlo predictions are normalised to the integrated luminosity of the data.

Monte Carlo. The principal decrease in efficiency is due to the charged event rejection. After the final selection 1.3 ± 0.5 background events are expected which is negligible compared to the expected $\gamma\gamma(\gamma)$ signal.

The efficiency and angular resolution of the reconstruction are determined using an $\mathcal{O}(\alpha^3)$ Monte Carlo sample with full detector simulation. In the angular range $\cos\theta^* < 0.8$ the efficiency is in the range 91 – 95% and drops to 40 % for $\cos\theta^* > 0.96$. The requirement with the lowest efficiency is the charged event rejection leading to a loss of events with early photon conversions.

To compare the conversion probability in data and Monte Carlo, a special event sample is selected. This sample consists of events with exactly 2 clusters, an acollinearity angle $\xi_{\text{acol}} < 5^\circ$ and an energy sum $E_S^I > 0.6\sqrt{s}$. At least one cluster must be consistent with a non-converted photon: neither a CV or a CJ token, nor a track with a minimum number of hits must be assigned to the cluster. This leads to a sample of 2810 unbiased clusters, where the cluster is selected via the opposite photon, i.e. all clusters, where the opposite cluster is consistent with a non-converted photon. This sample is used to study the probability that a CV or CJ token is assigned to a cluster. There are 13.5 ± 1.5 background events expected from Bhabha and multi-hadronic events in the angular range $\cos\theta^* < 0.8$. This may be compared to 14 events found by scanning the data after removing an additional 8 events originating from radiative return to J/Ψ . Concerning the single-veto probability, 51 clusters with both a CV and a CJ token assigned are found in the data, in agreement with the $\gamma\gamma(\gamma)$ Monte Carlo expectation of 44 clusters. Also for the double-veto probability for events that are not rejected by the single veto, a good agreement between data and Monte Carlo is observed: 41 clusters with either a CV or a CJ token assigned are found in the data while 40 are expected from Monte Carlo in the angular range $\cos\theta^* < 0.8$. In the angular range $\cos\theta^* < 0.97$ there are 258 clusters observed in the data and 248 expected from Monte Carlo. The study of the data alone leads to a 0.5% systematic error per cluster on the single-veto probability at $\cos\theta = 0$ due to the data statistics only. Including the information from the Monte Carlo, the overall systematic error on the efficiency is taken to be 1% at $\cos\theta = 0$, corresponding to 20% of the inefficiency; this value is used for all angles. The 1% error is taken to be correlated between all $\cos\theta^*$ bins.

The veto probability due to detector occupancy is determined from randomly triggered events. It is found to be 0.7% for the charged-event rejection (D) and 0.3% for the non-physics background rejection (B).

The agreement between generated and reconstructed event angles gives an event-angle resolution of about 0.2° . In addition, the cluster angle has been compared to the track angle for Bhabha events. For clusters with $|\cos\theta| > 0.96$, the cluster angle is systematically about 0.4° closer to the beam axis than the track angle. For clusters with $|\cos\theta| < 0.94$, the difference is less than 0.1° . Due to the cut-off at $\cos\theta^* < 0.97$ this would lead to a decrease of the measured total cross-section by 1.1% if this effect is caused by the cluster angle. It is included in the systematic error on the total cross-section.

The luminosity is derived from small-angle Bhabha scattering measured on both sides of the detector in the polar angle region $34 \text{ mrad} < \theta < 56 \text{ mrad}$. Uncertainties derive from the selection and the theoretical cross-section, as well as from a 20 MeV uncertainty on the beam energy. To be conservative and include additional uncertainties an increased systematic error

of 0.5% is taken into account for the final errors.

Since the deviations from QED (Equations 3 – 6) are given with respect to the Born level, the observed angular distribution is corrected to the Born level. The effect of radiative corrections is quantified by the ratio \mathcal{R} of the angular distribution of the $e^+e^- \rightarrow \gamma\gamma(\gamma)$ Monte Carlo and the Born-level cross-section:

$$\mathcal{R} = \left(\frac{d\sigma}{d\Omega} \right)_{\text{MC}} (\cos \theta^*) \bigg/ \left(\frac{d\sigma}{d\Omega} \right)_{\text{Born}} (\cos \theta^*) . \quad (9)$$

It is assumed that the higher-order corrections in the context of the studied models are equal to those expected from QED. The ratio \mathcal{R} varies between 1.03 and 1.06 within the studied angular range $\cos \theta^* < 0.97$ and is used to correct the data bin by bin to the Born level. A 1% systematic error from $\mathcal{O}(\alpha^4)$ and higher-order effects is taken to be correlated between all bins.

6 Results

Cross-section

In Table 3 the numbers of observed events in the different kinematic classes are compared to the Monte Carlo expectation after the final selection. Since there is no Monte Carlo generator for the case of four-photon events where at least one photon is along the beam axis, no prediction for class *IV* events with three observed photons is given. The prediction for events with four or more observed photons is calculated using FGAM. One class *IV* event with 4 detected photons is observed. Figure 3 shows a class *I* event with 4 detected photons, where the lowest-energy photon has an energy of 13.5 GeV. The expectation for a class *I* event with four photons with at least 10 GeV each is 0.07 events. The total cross-section σ for the process $e^+e^- \rightarrow \gamma\gamma(\gamma)$, determined from 1740 events selected in the range $\cos \theta^* < 0.97$, is also given in Table 3. The cross-section is corrected for detection efficiency, $\mathcal{O}(\alpha^3)$ effects derived from \mathcal{R} (Eq. 9) and the veto probability due to detector occupancy. The cross-section at the different LEP energies as measured by OPAL in the range $\cos \theta^* < 0.9$ is shown in Figure 4. All measurements are in good agreement with the QED prediction.

Class	<i>I</i>	<i>II</i>	<i>III</i>	<i>IV</i>		All	Cross-section [pb]	
N_γ	≥ 2	2	3	3	≥ 4	events	$\cos \theta^* < 0.9$	$\cos \theta^* < 0.97$
Observed	1587	125	20	7	1	1740	$7.55 \pm 0.18 \pm 0.14$	$11.4 \pm 0.3 \pm 0.3$
Expected	1612	131	32	–	0.8	1776	7.49	11.8

Table 3: Number of observed and expected events in the angular range $\cos \theta^* < 0.97$ for different classes. N_γ is the number of observed photon candidates. No Monte Carlo expectation is available for class *IV* events with 3 observed photons. The total cross-section is corrected to the Born level and is given for two angular ranges to allow comparison of these results with those of previous OPAL measurements. The first error is statistical, the second is systematic.

The angular distribution of the observed events and the measured differential cross-section obtained by applying efficiency and radiative corrections, are shown in Figure 5. The data have a $\chi^2/\text{NDF} = 14.8/20$ with respect to the QED expectation (solid line). The 95% CL interval of a χ^2 -fit to the data of the function $\left(\frac{d\sigma}{d\Omega}\right)_{\Lambda_{\pm}}$ (Eq. 3) is also shown (dashed line). To obtain the limits at 95% confidence level, the probability is normalised to the physically allowed region, i.e. $\Lambda_+ > 0$ and $\Lambda_- < 0$ as described in Ref. [20]. For both functions $\left(\frac{d\sigma}{d\Omega}\right)_{\Lambda_{\pm}}$ and $\left(\frac{d\sigma}{d\Omega}\right)_{\Lambda'}$ the χ^2 distribution is parabolic as a function of the chosen fitting parameters Λ_{\pm}^{-4} and Λ'^{-6} . The χ^2 distribution for $\left(\frac{d\sigma}{d\Omega}\right)_{G_{\pm}}$ from graviton exchange in the context of extra dimensions is also approximately parabolic. The asymmetric limits x_{95}^{\pm} on the fitting parameter are obtained by:

$$\frac{\int_0^{x_{95}^+} \Gamma(x, \mu, \sigma) dx}{\int_0^{\infty} \Gamma(x, \mu, \sigma) dx} = 0.95 \quad \text{and} \quad \frac{\int_{x_{95}^-}^0 \Gamma(x, \mu, \sigma) dx}{\int_{-\infty}^0 \Gamma(x, \mu, \sigma) dx} = 0.95, \quad (10)$$

where Γ is a Gaussian with the central value and error of the fit result denoted by μ and σ , respectively. This is equivalent to the integration of a Gaussian probability function as a function of the fit parameter. It is not possible to integrate the probability function as a function of Λ_{\pm} , Λ' or G_{\pm} . Therefore the limits on the fit parameters are derived via Eq. 10. The 95 % CL limits on the cut-off parameters are derived from the limits on the fit parameters, e.g. the limit on G_+ is obtained as $[x_{95}^+(G_{\pm}^{-4})]^{-1/4}$.

The limit on the mass of an excited electron M_{e^*} as a function of the coupling-constant ratio κ for the $(e^*e\gamma)$ -vertex, which is fixed during the fit, is shown in Figure 6. In the case of $\left(\frac{d\sigma}{d\Omega}\right)_{e^*}$ the cross-section does not depend linearly on the chosen fitting parameter $M_{e^*}^{-2}$ and the limit corresponds to an increase of the χ^2 by 3.84 with respect to the minimum.

The fit results are summarised in Table 4. Limits obtained from a combined fit to the data taken at 189 and 183 GeV are also given. The limits obtained are 30 – 115 GeV higher than our previous results [7].

Fit parameter	Fit result (189 GeV)	95% CL Limit [GeV]	
		189 GeV	183+189 GeV
Λ_{\pm}^{-4}	$(-36 \pm 71) \cdot 10^{-12} \text{ GeV}^{-4}$	$\Lambda_+ >$	297
		$\Lambda_- >$	304
Λ'^{-6}	$(-2.7 \pm 6.3) \cdot 10^{-18} \text{ GeV}^{-6}$	$\Lambda' >$	281
			295
G_{\pm}^{-4}	$(-1.7^{+3.2}_{-3.3}) \cdot 10^{-12} \text{ GeV}^{-4}$	$G_+ >$	674
		$G_- >$	672
$M_{e^*}^{-2}$	$(0.0 \pm 6.6) \cdot 10^{-6} \text{ GeV}^{-2}$	$M_{e^*} >$	660
			634
			311
			306

Table 4: Fit results and 95% CL lower limits obtained from the fit to the differential cross-section. The last column shows the limit obtained from a combined fit to the data taken at 183 and 189 GeV. The limit for the mass of an excited electron is determined assuming the coupling-constant ratio $\kappa = 1$.

Resonance production

A resonance X produced by the process $e^+e^- \rightarrow X\gamma$ and decaying into two photons, $X \rightarrow \gamma\gamma$, would be visible in the two-photon invariant mass spectrum, since this process leads to a three-photon final state without missing energy. Searches for such a resonance have been performed previously at the Z^0 peak [21] and at higher energies [7, 8, 22], leading to bounds on Higgs and gauge boson interactions [23]. For this search, 20 events from class *III* are used. The invariant mass of each photon pair is shown in Figure 7a). The energies of the three photons are not based on the measured cluster energies but are calculated from the photon angles assuming three-body kinematics:

$$E_k \propto \sin \alpha_{ij} ; E_1 + E_2 + E_3 = \sqrt{s}, \quad (11)$$

with E_k the energy of one photon and α_{ij} the angle between the other two photons. In this case, the typical mass resolution for photon pairs is about 0.5 GeV. Deriving the mass from the measured cluster energies would lead to a resolution of about 3%. The distribution is consistent with the Monte Carlo expectation from the QED process $e^+e^- \rightarrow \gamma\gamma(\gamma)$. There is no evidence for an enhancement due to a resonance.

An upper limit on the total production cross-section multiplied by the two-photon branching ratio is calculated using the method of Ref. [24]. This method uses fractional event counting where the weights assigned to each photon pair depend on the expected resolution and the difference between the hypothetical and the reconstructed mass. The limits shown in Figure 7b) are obtained assuming the natural width of the resonance to be negligible. The $e^+e^- \rightarrow \gamma\gamma(\gamma)$ background is subtracted. For the efficiency correction, the production and subsequent decay of the resonance are assumed to be isotropic. The mass range is limited by the acollinearity restriction. Regarding a model with anomalous couplings of the Higgs boson [23], this analysis gives access to a larger mass range than the analysis of $e^+e^- \rightarrow HZ$ with $H \rightarrow \gamma\gamma$ [25]. However, in the region of overlap the direct search is more sensitive.

7 Conclusions

The process $e^+e^- \rightarrow \gamma\gamma(\gamma)$ has been studied using data taken with the OPAL detector at centre-of-mass energies up to 189 GeV. The measured angular distribution and total cross-section for this process both agree well with QED predictions. The limits (95% CL) on cut-off parameters are $\Lambda_+ > 304$ GeV, $\Lambda_- > 295$ GeV and $\Lambda' > 672$ GeV. An excited electron is excluded for $M_{e^*} < 306$ GeV assuming the $e^*e\gamma$ and $ee\gamma$ coupling to be the same. Graviton exchange in the context of theories including extra dimensions is excluded for scales $G_+ < 660$ GeV and $G_- < 634$ GeV. In the $\gamma\gamma$ invariant mass spectrum of events with three final-state photons, no evidence is found for a resonance X decaying to $\gamma\gamma$. A limit on the production cross-section times branching ratio is derived as a function of the mass M_X .

Acknowledgements

We particularly wish to thank the SL Division for the efficient operation of the LEP accelerator at all energies and for their continuing close cooperation with our experimental group. We thank our colleagues from CEA, DAPNIA/SPP, CE-Saclay for their efforts over the years on the time-of-flight and trigger systems which we continue to use. In addition to the support staff at our own institutions we are pleased to acknowledge the
Department of Energy, USA,
National Science Foundation, USA,
Particle Physics and Astronomy Research Council, UK,
Natural Sciences and Engineering Research Council, Canada,
Israel Science Foundation, administered by the Israel Academy of Science and Humanities,
Minerva Gesellschaft,
Benozio Center for High Energy Physics,
Japanese Ministry of Education, Science and Culture (the Monbusho) and a grant under the Monbusho International Science Research Program,
Japanese Society for the Promotion of Science (JSPS),
German Israeli Bi-national Science Foundation (GIF),
Bundesministerium für Bildung, Wissenschaft, Forschung und Technologie, Germany,
National Research Council of Canada,
Research Corporation, USA,
Hungarian Foundation for Scientific Research, OTKA T-029328, T023793 and OTKA F-023259.

References

- [1] S.D. Drell, Ann. Phys. **4** (1958) 75.
- [2] F.A. Berends and R. Kleiss, Nucl. Phys. **B186** (1981) 22.
- [3] O.J.P. Éboli, A.A. Natale and S.F. Novaes, Phys. Lett. **B271** (1991) 274.
- [4] A. Litke, Ph.D.Thesis, Harvard University, unpublished (1970).
- [5] N. Arkani-Hamed, S. Dimopoulos and G. Dvali, Phys. Lett. **B429** (1998) 263;
I. Antoniadis, N. Arkani-Hamed, S. Dimopoulos and G. Dvali, Phys. Lett. **B436** (1998) 257;
N. Arkani-Hamed, S. Dimopoulos and G. Dvali, Phys. Rev. **D59** (1999) 86004.
- [6] OPAL Collaboration, K. Ackerstaff et al., Eur. Phys. J. **C1** (1998) 21.
- [7] OPAL Collaboration, K. Ackerstaff et al., Phys. Lett. **B438** (1998) 379.
- [8] L3 Collaboration, M. Acciarri et al., Phys. Lett. **B413** (1997) 159.
- [9] ALEPH Collaboration, R. Barate et al., Phys. Lett. **B429** (1998) 201.
- [10] DELPHI Collaboration, P. Abreu et al., Phys. Lett. **B433** (1998) 429.

- [11] OPAL Collaboration, K. Ahmet et al., Nucl. Instr. and Meth. **A305** (1991) 275.
- [12] CALCUL Collaboration, F.A. Berends et al., Nucl. Phys. **B239** (1984) 395;
P. Janot, PhD Thesis, LAL 87-31 (1987).
- [13] S. Jadach et al., Phys. Lett. **B390** (1997) 298.
- [14] D. Karlen, Nucl. Phys. **B289** (1987) 23.
- [15] S. Jadach et al., Comp. Phys. Comm. **66** (1991) 276.
- [16] J. Allison et al., Nucl. Instr. and Meth. **A317** (1992) 47.
- [17] I. Harris and L.M. Brown, Phys. Rev. **105** (1957) 1656;
F.A. Berends and R. Gastmans, Nucl. Phys. **B61** (1973) 414.
- [18] G.F. Giudice, R. Rattazzi and J.D. Wells, Nucl.Phys. **B544** (1999) 3.
- [19] OPAL Collaboration, M.Z. Akrawy et al., Phys. Lett **B257** (1991) 531.
- [20] Review of Particle Physics, C. Caso et al., Eur. Phys. J. **C3** (1998) 176.
- [21] OPAL Collaboration, P.D. Acton et al., Phys. Lett. **B311** (1993) 391;
L3 Collaboration, M. Acciarri et al., Phys. Lett. **B345** (1995) 609.
- [22] DELPHI Collaboration, P.Abreu et al., CERN-EP/99-58, submitted to Phys. Lett. B.
- [23] O.J.P. Éboli, M.C. Gonzalez-Garcia, S.M. Lietti and S.F. Novaes, Phys. Lett. **B434** (1998) 434.
- [24] P. Bock, Heidelberg preprint HD-PY 96/05.
- [25] OPAL Collaboration, G. Abbiendi et al., CERN-EP/99-084, submitted to Phys. Lett. B.

OPAL

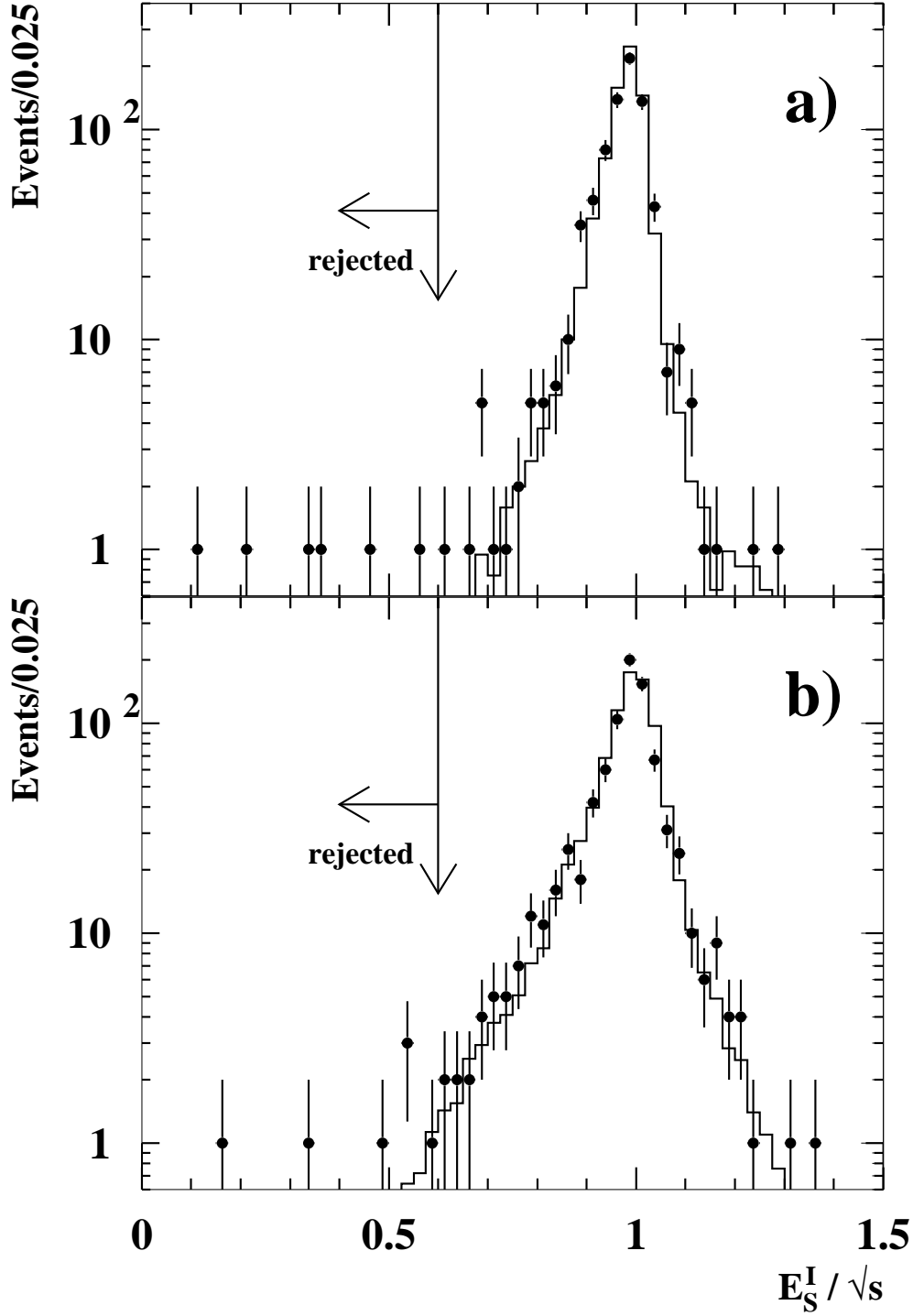


Figure 1: Scaled energy sum E_s^I / \sqrt{s} for class *I* events. a) shows events with $\cos \theta^* < 0.8$ and b) shows events with $\cos \theta^* > 0.8$. The points show the data and the histogram represents the Monte Carlo expectation, normalised to the integrated luminosity of the data. The cut is indicated by an arrow.

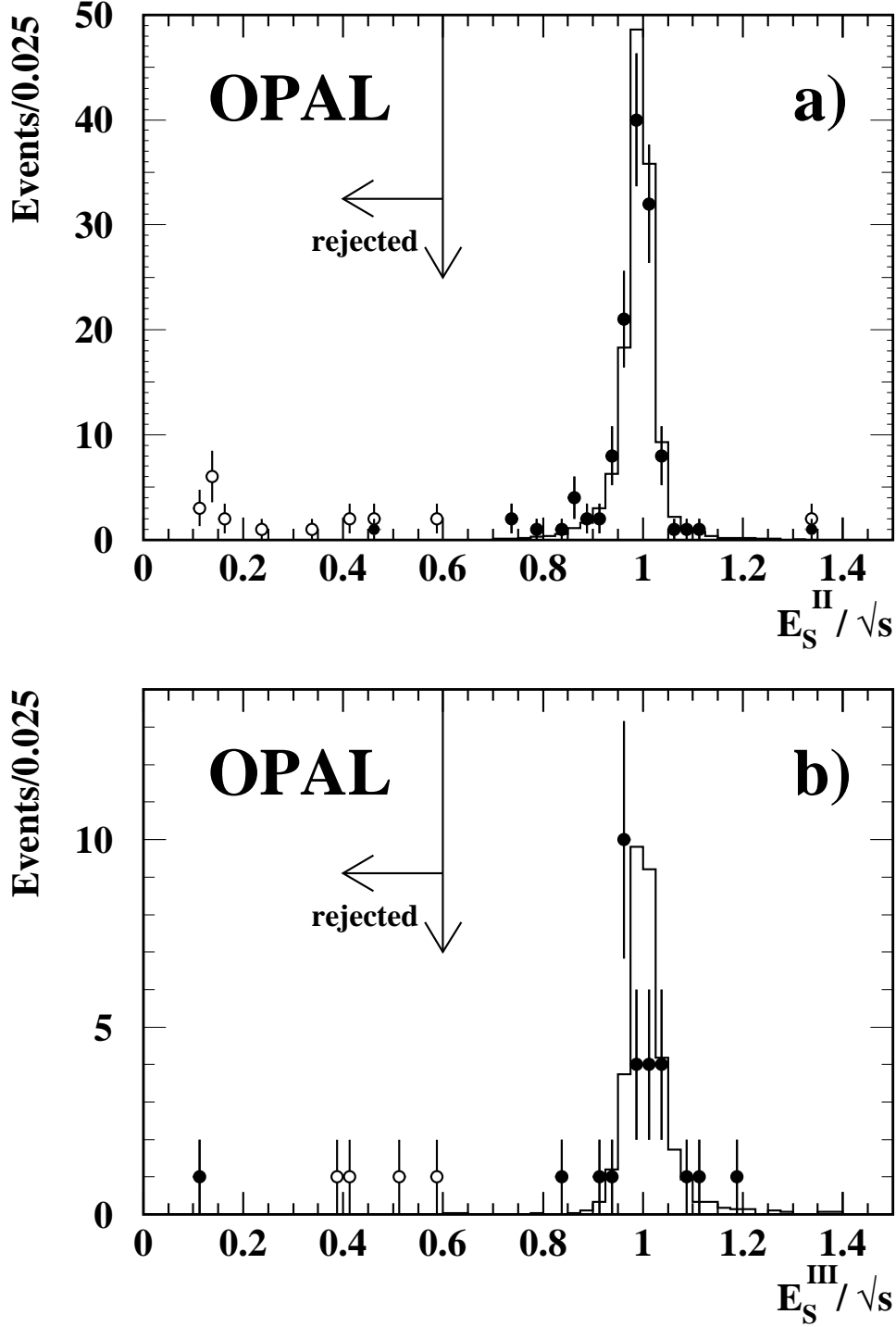


Figure 2: a) Scaled energy sum $E_s^{\text{II}} / \sqrt{s}$ for class II events after the cut on E_{lost} . b) Scaled energy sum $E_s^{\text{III}} / \sqrt{s}$ for class III and IV events after the cut on p_t . The solid points show the data after the cut on the imbalance \mathcal{B} (Fig. a) and the transverse momentum p_t (Fig. b), and the open points show the data suppressed by these requirements. The histogram represents the Monte Carlo expectation, normalised to the integrated luminosity of the data. The Monte Carlo distribution is shown after the cuts with have negligible effect. The cut is indicated by an arrow.

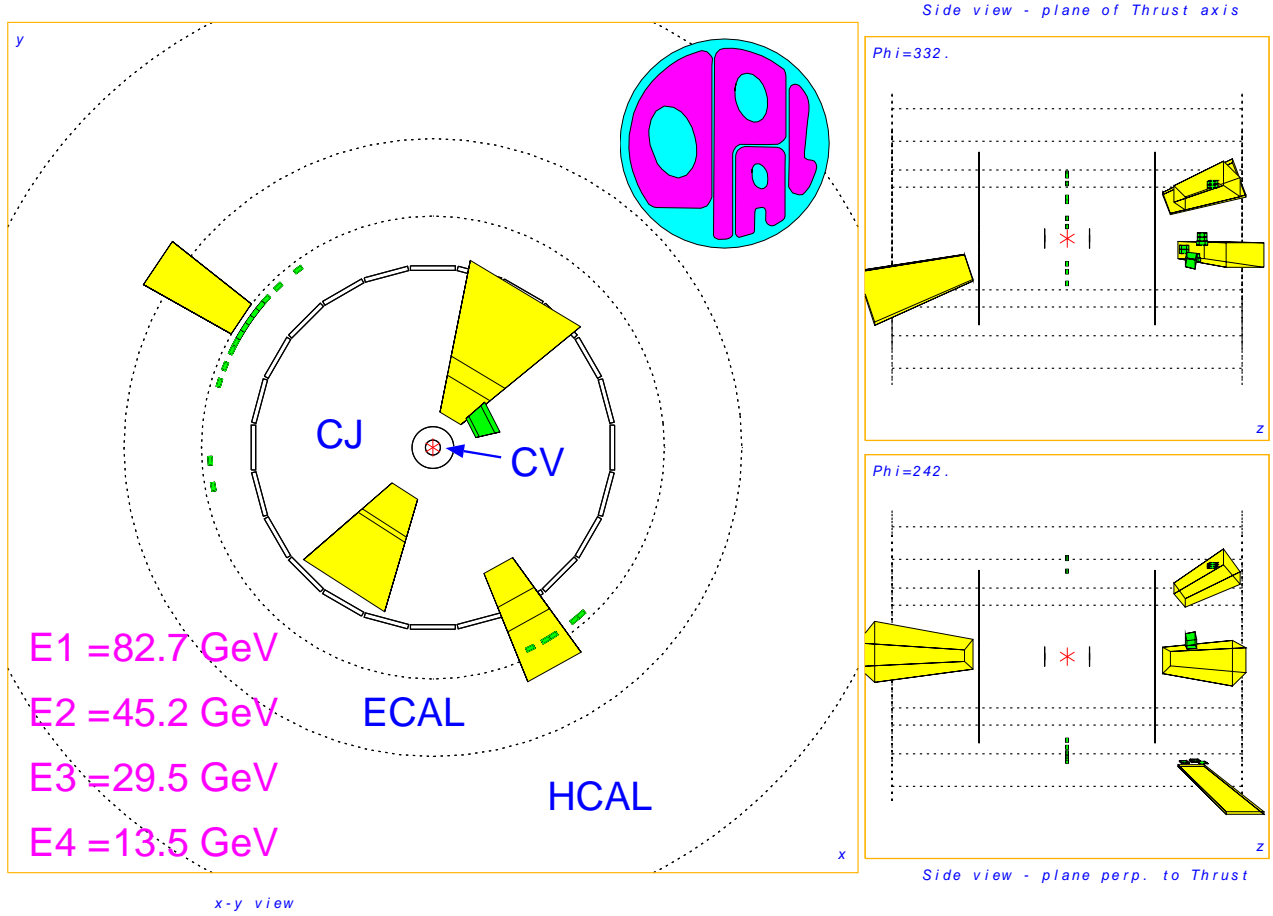


Figure 3: Display of an event with four detected photons. Reconstructed clusters in the ECAL are shown as blocks where the size is proportional to the energy deposit. Since the two highest energy photons have an acollinearity of 3.9° it is selected as class *I* event. There are 0.07 events expected in class *I* with four photons with an energy of more than 10 GeV each.

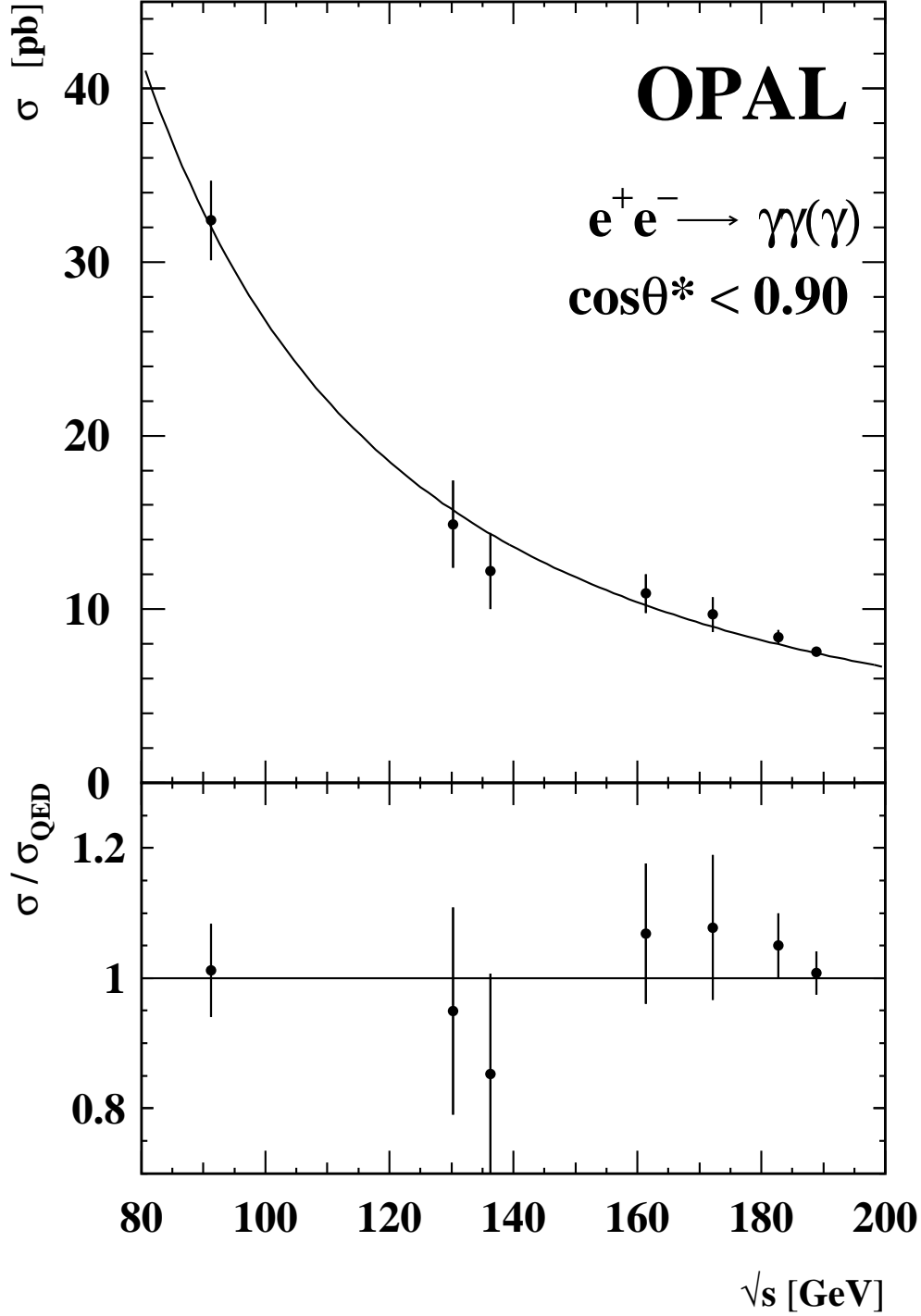


Figure 4: Total cross-section for the process $e^+e^- \rightarrow \gamma\gamma(\gamma)$ with $\cos\theta^* < 0.9$. The curve corresponds to the Born-level QED expectation. The lower plot shows the distribution normalised to the QED expectation. The data are corrected for efficiency loss and higher-order effects and correspond to the Born level. Results at lower energies are taken from previous OPAL publications [6, 7, 19].

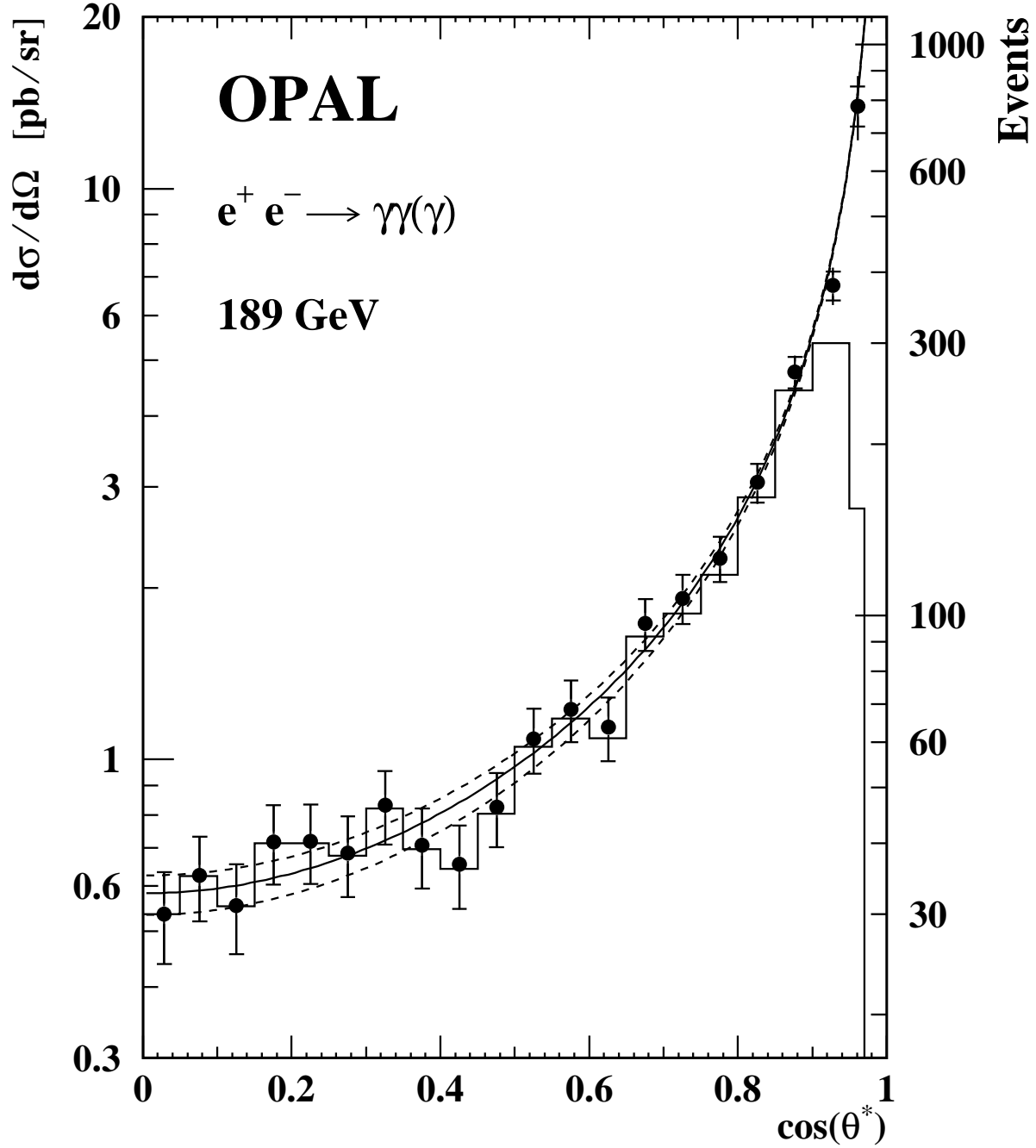


Figure 5: The measured angular distribution for the process $e^+e^- \rightarrow \gamma\gamma(\gamma)$ at $\sqrt{s} = 189$ GeV. The histogram shows the observed number of events per bin. Note the smaller width of the highest $\cos\theta^*$ bin. The points show the number of events corrected for efficiency and radiative effects. The inner error-bars correspond to the statistical error and the outer error-bars to the total error. The solid curve corresponds to the Born-level QED prediction. The dashed lines represent the 95% CL interval of the fit to the function $\left(\frac{d\sigma}{d\Omega}\right)_{\Lambda_{\pm}}$.

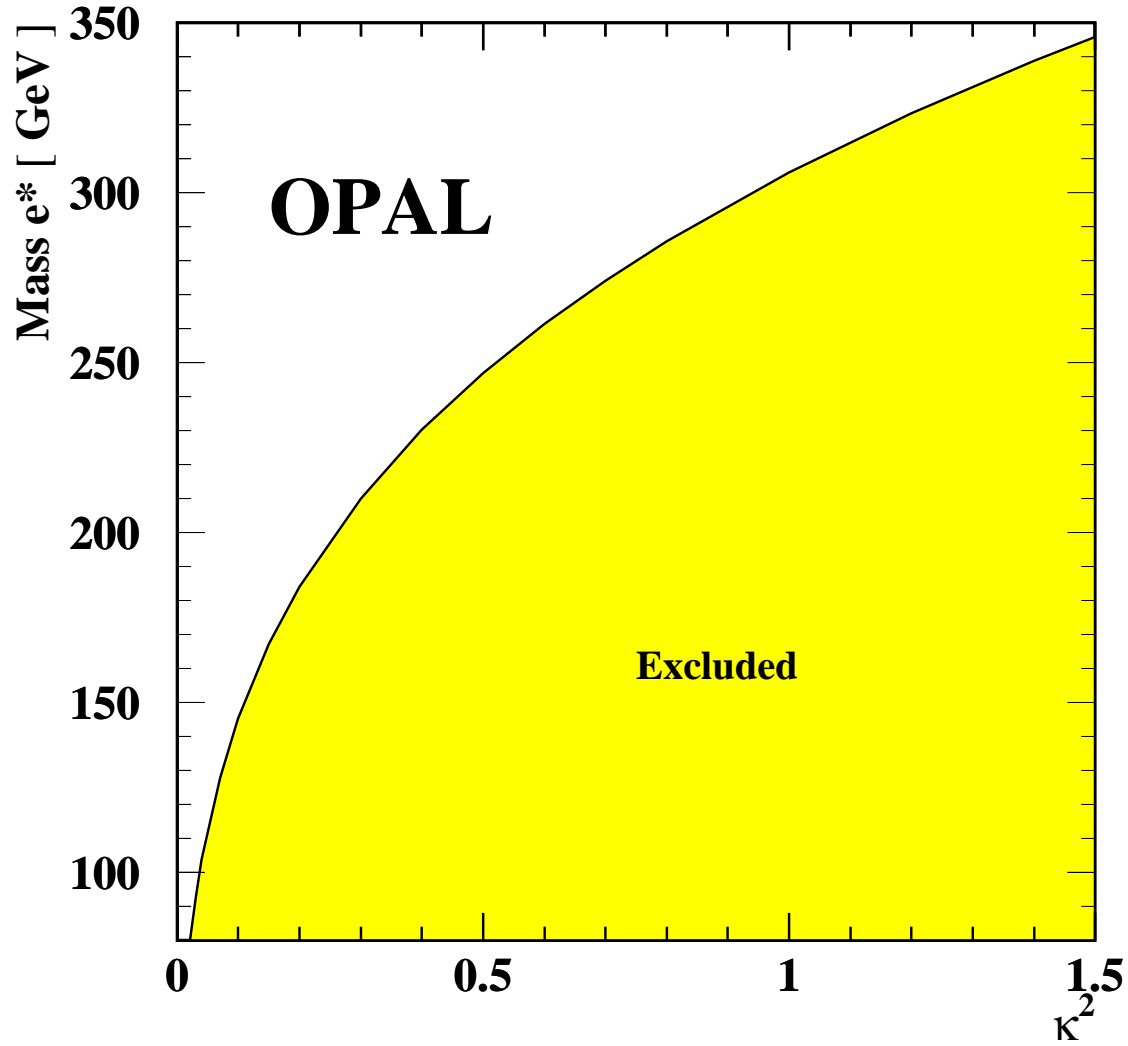


Figure 6: Lower limit (95% CL) on the mass M_{e^*} of an excited electron as a function of the square of the $e^*\gamma$ coupling constant ratio κ^2 obtained from a combined fit to data taken at 183 and 189 GeV.

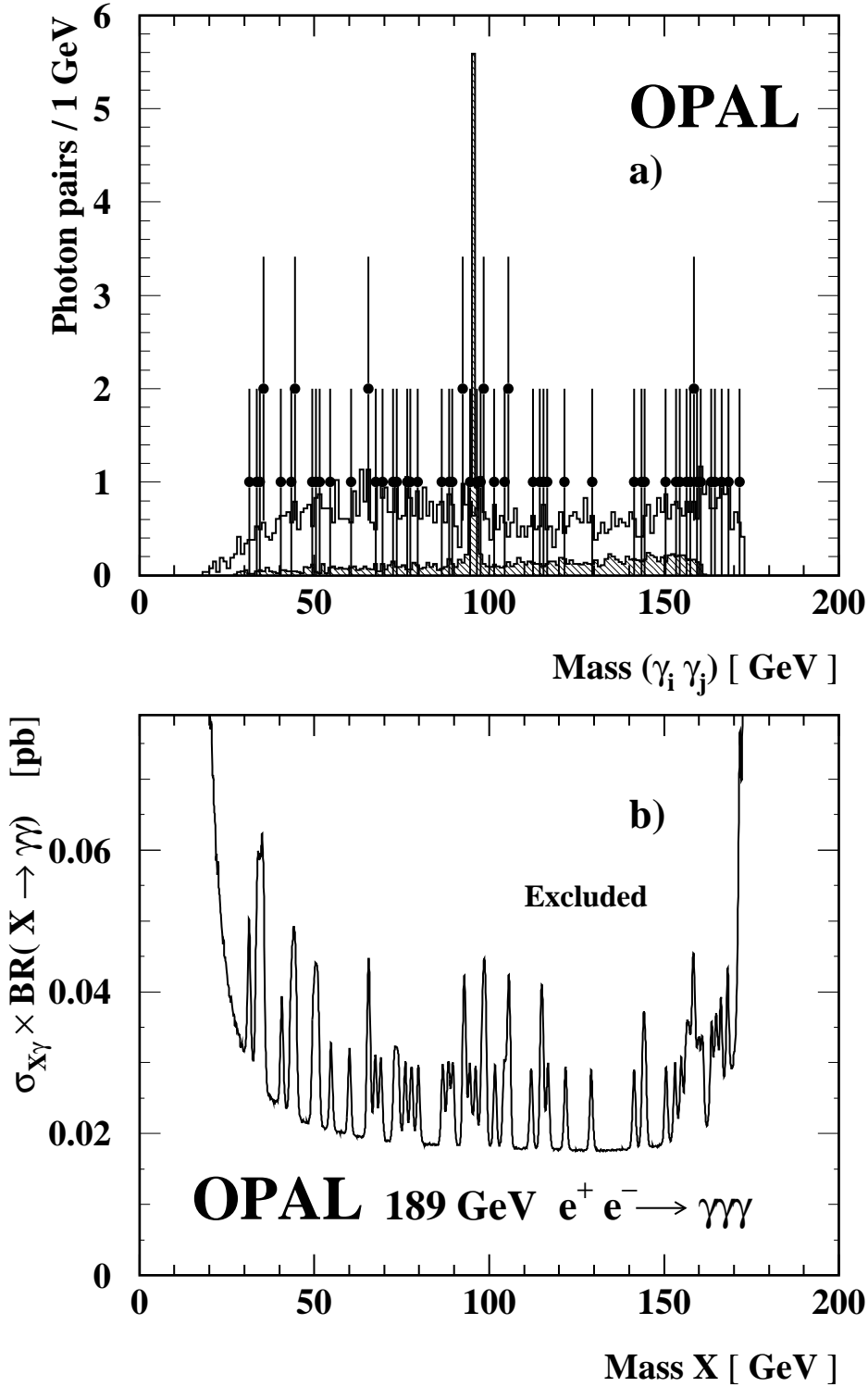


Figure 7: Results of a search for resonance production in class *III* events. a) shows the invariant mass of photon pairs for data (points) and for the $e^+e^- \rightarrow \gamma\gamma(\gamma)$ Monte Carlo expectation (open histogram). The hatched histogram represents a $\gamma\gamma$ resonance at 95.5 GeV with a cross-section times branching ratio of 0.05 pb. The binning is chosen to match the expected mass resolution. b) shows the upper limit (95% CL) for the cross-section times branching ratio for the process $e^+e^- \rightarrow X\gamma$, $X \rightarrow \gamma\gamma$ as a function of the mass of the resonance X .